

Ray-driven Spectral CT Reconstruction Based on Neural Base-Material Fields

Ligen Shi*, Chang Liu†, Ping Yang*, Jun Qiu† and Xing Zhao*‡

*School of Mathematical Science, Capital Normal University, Beijing 100048, China

†Institute of Applied Mathematics, Beijing Information Science and Technology University, Beijing 100101, China

‡zhaoxing_1999@126.com

Abstract—In spectral CT reconstruction, the basis materials decomposition involves solving a large-scale nonlinear system of integral equations, which is highly ill-posed mathematically. This paper proposes a model that parameterizes the attenuation coefficients of the object using a neural field representation, thereby avoiding the complex calculations of pixel-driven projection coefficient matrices during the discretization process of line integrals. It introduces a lightweight discretization method for line integrals based on a ray-driven neural field, enhancing the accuracy of the integral approximation during the discretization process. The basis materials are represented as continuous vector-valued implicit functions to establish a neural field parameterization model for the basis materials. The auto-differentiation framework of deep learning is then used to solve the implicit continuous function of the neural base-material fields. This method is not limited by the spatial resolution of reconstructed images, and the network has compact and regular properties. Experimental validation shows that our method performs exceptionally well in addressing the spectral CT reconstruction. Additionally, it fulfils the requirements for the generation of high-resolution reconstruction images.

Index Terms—Base material decomposition, Neural base-material field, Neural field, Spectral CT reconstruction

I. INTRODUCTION

COMPUTED Tomography (CT) is a widely used imaging technology in modern medical diagnostics and industrial inspection. It is valued for its fast scanning speeds and ability to produce high-fidelity reconstructed images. In medical and industrial CT applications, X-ray sources operate by accelerating electrons that collide with tungsten (or molybdenum or similar materials) targets, resulting in the emission of X-ray photons across a range of energies. The distribution of photon counts at different energies follows a specific probability distribution curve known as the X-ray spectrum.

Traditional CT reconstruction algorithms typically do not consider the X-ray spectrum. The CT values in their reconstructed images represent a nonlinear average of the attenuation coefficients of X-ray photons with different energies for each pixel. This averaging process can lead to similar or even identical CT values for substances with low density and high atomic numbers, as well as substances with high density and low atomic numbers. This may also lead to inherent image artefacts in CT images, such as beam hardening and streak

artefacts. Various dual-spectrum and multi-spectrum CT imaging modes have been proposed to address these image artefacts and improve CT's ability to identify and quantitatively analyze object compositions.

Spectral CT uses X-ray scans with multiple spectra or different energy levels within a single spectrum to scan an object. This allows it to take advantage of the varying absorption properties of the object for X-rays at various energies. As a result, it acquires a more extensive and detailed dataset compared to conventional CT.

Kalender et al. [1] introduced the basis material decomposition model for spectral CT. This model aims to reconstruct density images of base materials and generate pseudo-monochromatic images by combining them, effectively reducing artefact effects [2]. The challenge of basis material decomposition in spectral CT involves solving a complex and large-scale nonlinear integral equation system. This system is inherently ill-conditioned due to similarities in the variations of mass attenuation coefficients for different base materials with X-ray energy (in keV units). Moreover, the ill-conditioning is exacerbated by the fact that as the radiation passes through highly attenuating substances, there is a higher statistical error in the measurement data of low-energy photons compared to those at higher energies. The ill-conditioning of the equation system amplifies noise during the basis material decomposition process, making it susceptible to noise interference and various artefacts.

Recent research has shown that Multilayer Perceptrons (MLPs), deep fully connected neural networks, have great potential to represent complex low-dimensional signals [3]. Unlike traditional methods that rely on discretely sampled arrays, coordinate-based neural representations offer a continuous alternative that overcomes the limitations of fixed spatial resolution. Therefore, we utilize MLPs with activation functions to represent the base materials. This method uses neural networks to parameterize these materials' continuous 3D vector-valued implicit functions. We refer to this parameterized form as the neural base-material fields. To address the

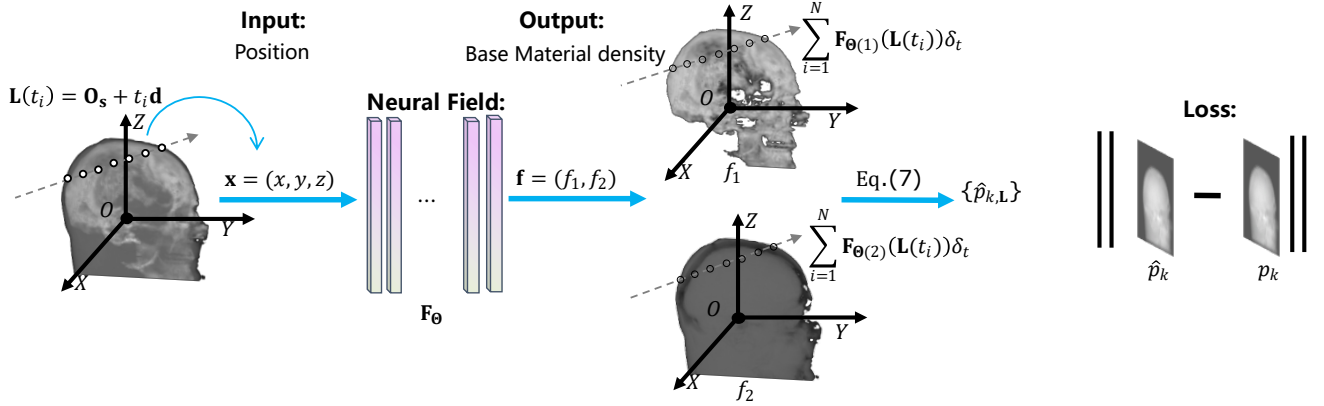


Fig. 1. Framework diagram of polychromatic projections for dual-material decomposition based on neural base-material fields. The network takes the coordinates $\mathbf{x} = (x, y, z)$ of sampling points along the ray $\mathbf{L}(l)$ as input and predicts the corresponding material densities $\mathbf{f} = (f_1, f_2)$. The network predicts the density that corresponds to this sampling point coordinates on the ray $\mathbf{L}(l)$ and calculates the polychromatic projection values $\hat{p}_{k,L}$ along the path of \mathbf{L} under the k -th spectrum using Eq.(7). The loss between $\hat{p}_{k,L}$ and the true projection p_k is computed for backpropagation.

forward problem in spectral CT, we establish a discretization model based on these neural base-material fields. We also leverage their differentiability to tackle the inverse problem. By doing so, we convert the task of material decomposition in spectral CT into an optimization problem involving the neural base-material fields.

This approach eliminates the need to solve large-scale sparse system matrices. Figure 1 illustrates the framework of our method implicit representation of base materials using coordinate-based neural networks. The primary contributions of this study can be summarized as follows:

- 1) A model is proposed to parameterize the attenuation coefficients using neural fields, aiming to avoid the complex computations of pixel-driven projection coefficient matrices in the discretization process of line integration. A lightweight line integral discretization method is introduced based on neural fields driven by rays.
- 2) Based on the implicit representation framework of base materials, an optimization solution model for the non-linear inverse problem of materials based on neural fields is established. Leveraging the auto-differentiation framework of deep learning, the network is endowed with the ability to learn real material densities, thus enabling the training of a continuous material density model.

II. RELATED WORK

This section provides an overview of the main methods used for base material decomposition in spectral CT and recent advancements in the neural field.

A. Base Material Decomposition in Spectral CT Imaging

Direct image domain decomposition algorithms are based on conventional reconstruction techniques such as the Simultaneous Algebraic Reconstruction Technique (SART) and Filtered Back Projection (FBP), where polychromatic projection data is directly reconstructed into images, and subsequently mapped to base material images through inverse transformations. This approach is known as the Brooks method [4]. However, it has limitations as it assumes monochromatic projections and does not account for the polychromatic nature of X-rays. This leads to artefacts such as cupping and streaking [5], [6]. To mitigate these effects, prior corrections or polynomial approximations are typically used [7], [8].

Projection domain direct mapping methods in spectral CT convert polychromatic projection data into monochromatic projections corresponding to each base material. Separate reconstructions are then performed using traditional algorithms like SART and FBP. Due to the complex interactions between radiation and materials, this approach involves modelling non-linear functions, spectral characteristics, detector responses, noise models, and energy-dependent mass attenuation coefficients of materials. To simplify the process, researchers often use lookup tables [9], polynomial fittings [10], [11], or piecewise polynomials [12]. While these methods require fewer parameters and are relatively easy to calibrate, their accuracy is inherently limited by the expressiveness of the approximation and discrepancies between calibration phantoms and actual complex objects.

Iterative decomposition algorithms address the challenges of nonlinear mapping in spectral CT, particularly in scenarios with scanning paths that lack geometric consistency. One

such algorithm, E-ART [13], rectifies polychromatic projections into monochromatic projections of base materials and updates the base material images using consistency conditions. This approach effectively tackles projection-domain reconstruction under inconsistencies. Although iterative methods require more computational resources, they offer superior noise suppression capabilities and improved results when combined with physical models. Several subsequent algorithms have been developed to improve convergence rates [14]–[16]. Notably, the IFBP [15] takes advantage of high- and low-spectra data to enhance residual projection calculations and accelerate convergence in cases of geometrical inconsistency. First, weighted residuals from polychromatic projections are computed and then reconstructed via FBP in the image domain. Subsequently, corrected base material images are generated by leveraging pixel-wise correspondences within the image domain. This method successfully overcomes projection inconsistencies and enhances decomposition precision.

Learning-based methods are increasingly recognized as practical tools for spectral CT base material decomposition. Several studies have successfully employed deep learning frameworks to simulate the complex nonlinear relationship between high and low- spectral projection values and material decomposition coefficients. For instance, references [17], [18] utilize deep learning to fit this relationship, while [19] introduces a butterfly network architecture to map reconstructed images to material decomposition images. [20] explores linear mapping relationships using U-Net, and [21] leverages generative adversarial networks (GAN) to generate material decomposition images. [22] directly maps reconstructed images from high and low-spectra to material decomposition coefficient images using convolutional neural networks. Additionally, [23] employs ResNet to generate pseudo-monochromatic images at different energies and further computes base material decomposition images. Deep learning inherently provides more powerful mathematical modelling methods, but its reconstruction accuracy relies on large-scale annotated datasets. Nevertheless, procuring labelled data entails substantial effort and frequently encounters difficulties across various contexts.

B. Scene Representations and Neural Field

NeRF [3] introduces a novel approach to view synthesis by utilizing deep fully connected neural networks, also known as multilayer perceptrons (MLPs), for volume rendering and implicit neural scene representation. This method achieves state-of-the-art visual quality and has inspired numerous subsequent works [24], [25]. Recent research has demonstrated the potential of MLPs in representing complex low-dimensional signals such as occupancy, density, colour, SDF, etc. [26].

A coordinate-based neural representation MLP, with weights Θ , is optimized to map input coordinates \mathbf{x} to corresponding signal values. The main advantage of this representation is that the signal or field it represents is implicitly defined by the given coordinates. Unlike signals stored in discrete numerical arrays, coordinate-based neural representations are continuous and not limited by fixed spatial resolutions. Several coordinate-based neural network methods [27]–[33] have recently emerged for CT reconstruction, demonstrating excellent performance.

The problem of material decomposition in spectral CT involves solving a large-scale nonlinear system of integral equations, which is highly ill-conditioned. Moreover, standard algorithms struggle to reconstruct high-resolution CT images. To address these challenges, this paper adopts a novel computational imaging approach that uses a coordinate-based implicit neural network representation to parameterize base material images. This method is self-supervised and does not require external datasets for training.

III. NEURAL BASE-MATERIAL FIELDS

In this section, we provide a detailed overview of our method. Figure 1 illustrates the general workflow of our approach. Our method represents the decomposed base materials as a continuous 3D vector-valued function. Using neural base-material fields, we parametrize the base materials as MLPs with activation functions. Furthermore, we introduce a discretization model for the forward process of base material decomposition polychromatic projections, which is based on the neural base-material fields. In addition, we have developed a method to solve the inverse problem of the neural base-material fields using an automatic differentiation framework.

A. Models for Base Material Decomposition

In the context of considering the X-ray photon spectrum and neglecting scattered photons, the measured data of polychromatic projections $p_k(\mathbf{L})$ along the path of the ray \mathbf{L} scanning the object can be mathematically modelled as follows:

$$p_k(\mathbf{L}) = -\ln \int S_k(E) e^{-\int_{\mathbf{L}} \mu(\mathbf{x}, E) dl} dE, \quad (1)$$

$$\mathbf{L} \in \Pi_k, k = 1, 2, \dots, K$$

where $S_k(E)$ represents the normalized equivalent spectrum for the k -th spectrum; $\mu(\mathbf{x}, E)$ denotes the linear attenuation coefficient of photons at position \mathbf{x} for energy E ; Π_k is the set of scanning ray paths for the k -th spectrum.

During the reconstruction of spectral CT, the unknown function $\mu(\mathbf{x}, E)$ is to be determined. Since directly solving for the unknown function from the collected projection data is ill-posed, dimensionality reduction of the unknowns is necessary.

To achieve this, the linear attenuation coefficients of materials are approximated as a combination of M basis functions:

$$\mu(\mathbf{x}, E) \approx \sum_{m=1}^M \theta_m(E) f_m(\mathbf{x}), \quad (2)$$

where $\theta_m(E)$ represents pre-calibrated basis functions, and $f_m(\mathbf{x})$ denotes the coefficients of the basis functions. Thus, the reconstruction problem in spectral CT is transformed from solving for $\mu(\mathbf{x}, E)$ to solving for $f_m(\mathbf{x})$.

The basis material decomposition model in spectral CT [1] suggests setting the basis functions as the mass attenuation coefficients of the m -th material, i.e., $f_m(E) = \mu_m(E)$, aiming to reconstruct the distribution images of the corresponding basis materials $f_m(\mathbf{x})$. Substituting Eq.(2) into Eq.(1), the forward process of the basis material decomposition polychromatic projection model is obtained:

$$p_k(\mathbf{L}) = -\ln \int S_k(E) e^{-\sum_{m=1}^M \theta_m(E) \int_L f_m(\mathbf{x}) d\mathbf{l}} dE, \quad (3)$$

$$\mathbf{L} \in \Pi_k, k = 1, 2, \dots, K.$$

The problem of spectral CT based on basis material decomposition involves reconstructing the density images $f_m(\mathbf{x})$, $m = 1, 2, \dots, M$ of various basis materials from the polychromatic projection $p_k(\mathbf{L})$ for each spectrum $k = 1, 2, \dots, K$.

B. Parametric Modeling of Neural Base-Material Fields

We decompose the density and structural information of objects using M base materials, representing the decomposed base materials as a continuous 3D vector-valued implicit function $\mathbf{f}(\mathbf{x})$. To achieve this, we employ a neural network model \mathbf{F}_Θ constructed by MLPs to fit this continuous 3D vector-valued implicit function, referred to as the neural base-material fields. The network takes 3D coordinate positions $\mathbf{x} = (x, y, z)$ as input and outputs M base material density maps $\mathbf{f}(\mathbf{x}) = (f_1(\mathbf{x}), f_2(\mathbf{x}), \dots, f_M(\mathbf{x}))$. The network's operation can be mathematically expressed as:

$$\mathbf{F}_\Theta : \mathbf{x} \rightarrow \mathbf{f}(\mathbf{x}). \quad (4)$$

The weights Θ are optimized to ensure that each input 3D coordinate is accurately mapped to its corresponding base material density.

C. Discretization of the Forward Process for Neural Base-Material Fields

In this section, we present the forward model of the polychromatic projection for material decomposition based on neural base-material fields:

$$p_k(\mathbf{L}) = -\ln \int S_k(E) e^{-\sum_{m=1}^M \theta_m(E) \int_L \mathbf{F}_{\Theta(m)}(\mathbf{x}) d\mathbf{l}} dE, \quad (5)$$

$$\mathbf{L} \in \Pi_k, k = 1, 2, \dots, K.$$

where $\mathbf{F}_{\Theta(m)}$ denotes the density values of the m -th channel output by the \mathbf{F}_Θ network.

We discretize the X-ray spectrum and path to numerically estimate the continuous integral in Eq.(5). For the k -th spectrum, it is uniformly divided into Ω_k intervals with an energy interval of δ_E , and sampling is performed for $S_k(E)$ and $\theta_m(E)$ within each energy interval to achieve spectrum discretization.

To discretize the X-ray path numerically and describe the relationship between the X-ray source and the detector, we construct a coordinate system as shown in Fig.2. When rotating counterclockwise by an angle ϕ , the corresponding rotation matrix is $\Phi(\phi) = \begin{bmatrix} \cos \phi & -\sin \phi & 0 \\ \sin \phi & \cos \phi & 0 \\ 0 & 0 & 1 \end{bmatrix}$. The coordinates of the X-ray source focus \mathbf{O}_s at angle $\phi = 0^\circ$ are $[0, SOD, 0]^T$, and the unit vector \mathbf{d} of the X-ray at this angle can be calculated from the X-ray source to the detector unit direction, expressed as $\mathbf{d} = [\frac{u}{\sqrt{u^2+v^2+SDD^2}}, \frac{-SDD}{\sqrt{u^2+v^2+SDD^2}}, \frac{v}{\sqrt{u^2+v^2+SDD^2}}]^T$. Therefore, any X-ray can be represented as:

$$\mathbf{L}(t) = \mathbf{O}_s + t\mathbf{d}. \quad (6)$$

At any angle ϕ , Eq.(6) only needs to be multiplied by the rotation matrix $\Phi(\phi)$ to obtain the representation of the X-ray at that angle.

Within the interval defined by the radius of the visual circle extended along the X-ray direction vector \mathbf{d} , ranging from $R - SOD$ to $R + SOD$, each X-ray path undergoes uniform discrete sampling with a constant step δ_t . This process yields precisely N sampling points along each ray. By multiplying the values of the N sampling points by the sampling step, we discretize the X-ray. Therefore, Eq.(5) can be transformed into the following discrete form:

$$p_{k,\mathbf{L}} = -\ln \sum_{E=1}^{\Omega_k} S_{k,E} \delta_E e^{-\sum_{m=1}^M \theta_m(E) \sum_{i=1}^N \mathbf{F}_{\Theta(m)}(\mathbf{L}(t_i)) \delta_t}, \quad (7)$$

$$\mathbf{L} \in \Pi_k, k = 1, 2, \dots, K.$$

where $S_{k,E}$ and $\theta_{m,E}$ represent the sampling values of $S_k(E)$ and $\theta_m(E)$ in the E -th subinterval, respectively.

D. Inverse Problem Solving for neural base-material fields

We optimize the network parameters Θ by minimizing the l_1 norm between the predicted projection $\hat{p}_{k,\mathbf{L}}$ and the ground truth $p_{k,\mathbf{L}}$ of the ray \mathbf{L} :

$$\Theta^* = \arg \min_{\Theta} \frac{1}{|\Pi_k|} \sum_{\mathbf{L} \in \Pi_k} \|\hat{p}_{k,\mathbf{L}} - p_{k,\mathbf{L}}\|_1, \quad (8)$$

where Π_k is the set of rays under spectrum k .

Although MLPs are universal function approximators [34], their main drawback is their poor performance in learning

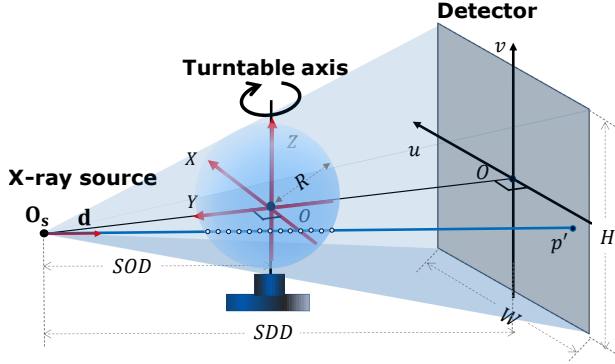


Fig. 2. Diagram illustrating the sampling points of X-rays. A right-handed coordinate system is established with the intersection point of the turntable axis and the perpendicular line from the X-ray source S to the rotation axis as the origin. The Z axis is parallel to the rotation axis, and the Y axis points towards the X-ray source. Ouv represents the detector coordinate system, where the u -axis and v -axis are parallel to the rows and columns of the detector, respectively, with the origin located at the centre of the detector. The line labelled p' represents a ray at a certain angle. SOD denotes the distance from the X-ray source to the rotation centre, SDD denotes the distance from the X-ray source to the detector, and H and W represent the height and width of the detector. The radius R of the Field of View is calculated as $R = \frac{SOD \cdot 0.5 \cdot \min(H, W)}{\sqrt{SDD^2 + (0.5 \cdot \min(H, W))^2}}$.

high-frequency content [35]. Solutions have been proposed in the literature, such as [36]–[38]. We utilize positional encoding as proposed in [36], restructuring \mathbf{F}_Θ into a composite of two functions: $\mathbf{F}_\Theta = \mathbf{F}'_\Theta \circ \gamma$. This composition includes standard MLPs and a Fourier feature mapping. The encoding function $\gamma(p)$ is defined as follows:

$$\gamma(p) = (\sin(2^0 \pi p), \cos(2^0 \pi p), \dots, \sin(2^{D-1} \pi p), \cos(2^{D-1} \pi p)), \quad (9)$$

where $\gamma(\cdot)$ is applied to each of the three coordinate values in \mathbf{x} normalized to lie within $[-1, 1]$, and D is the dimensionality of the encoding.

To train the neural base-material field model, the following steps are performed:

- Along the X-ray direction \mathbf{d} , uniformly sample N points within the distance interval of $[R - SOD, R + SOD]$ using a fixed step size equivalent to half a pixel length.
- Input the sampled points encoded by positional encoding into the network and compute the corresponding polychromatic projection values according to Eq.(7).
- Calculate the loss between the predicted projection values and the ground truth values, and through backpropagation, enable the network to learn the true material densities, thus training a continuous material density model.

IV. EXPERIMENTS

In this section, we use simulated data to evaluate the performance of our method in dual-spectral dual-material decomposition under various conditions. These conditions

include noise-free, sparse angles, poisson noise, and geometric inconsistency. We also provide experimental validation of the algorithm's effectiveness in handling ill-posed and underdetermined equation systems through single spectral dual-material decomposition. Additionally, we demonstrate the algorithm's excellent performance in high-resolution reconstruction by extracting images at different resolutions. For simplicity, all experiments in this section are conducted using fan-beam CT. The network architecture is shown in Fig. 3. It is worth noting that extending our method to cone-beam CT is straightforward. We quantitatively evaluate the algorithm's performance using peak signal-to-noise ratio (PSNR) and structural similarity index measurement (SSIM).

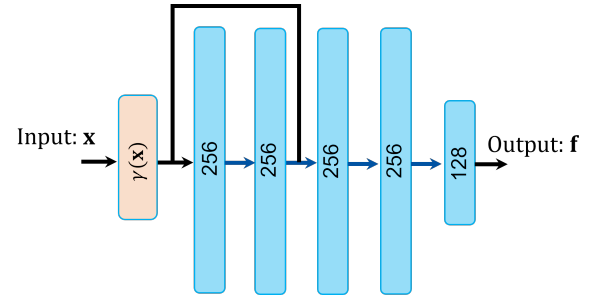


Fig. 3. The architecture diagram illustrates the fan-beam neural base-material fields. Hidden layers, depicted in blue, indicate the vector dimensions within each block; blue arrows denote connections to ReLU activation functions, while black skip connections represent residual or shortcut connections.

A. Dual-Spectral Dual-Material Decomposition Experiments

This section uses dual-spectrum X-ray scanning to reconstruct dual-material images, where $M = K = 2$. Both the E-SART and IFBP algorithms belong to iterative methods, exhibiting robust noise resistance and are suitable for scenarios with geometric inconsistencies in the scanning paths and different spectra. Therefore, this paper compares our method with the E-SART and IFBP algorithms to validate its performance.

Experiment Setups The experiments use slice data from the 3D FORBILD thorax phantom. Figure 4(a) illustrates the thorax phantom with a resolution of 512×512 . For detailed thorax phantom information, please refer to <https://web.archive.org/web/20070611224607/http://www.imp.uni-erlangen.de/forbild/deutsch/results/thorax/thorax.htm>. The thorax phantom is composed of materials with varying densities, such as water and bone. Water and bone are also used as the base materials for image reconstruction. The mass attenuation coefficients of the materials (water and bone) are obtained from NIST (see: <https://www.nist.gov/pml/x-ray-mass-attenuation-coefficients>).

The X-ray spectra used in the experiment were simulated using the free software SpectrumGUI (see <https://sourceforge.net/projects/spectrumgui/>). The X-ray

source is the GE Maxiray 125 X-ray tube, with voltages of 80 kV and 140 kV, the latter filtered by 1mm copper. Figure 4(b) illustrates the normalized X-ray spectra.

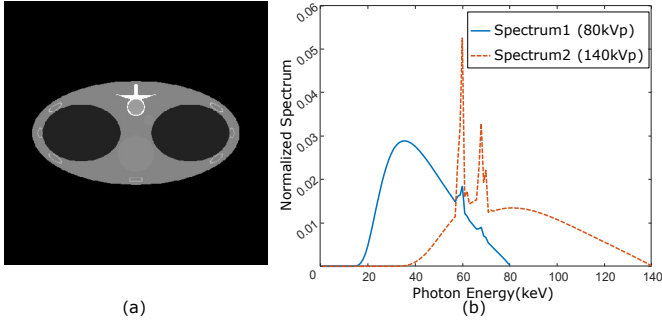


Fig. 4. (a) Slice of the thorax phantom used in the numerical simulation; (b) X-ray spectra used in the numerical simulation.

Scanning Configuration The distance between the X-ray source and the rotation centre (Turntable axis) is $SOD = 1000$ mm, and the distance between the X-ray source and the detector is $SDD = 1536$ mm. The linear detector consists of 512 detection units, with each unit’s size being 0.8 mm. Polychromatic projections are obtained through Eq.(7).

With the above parameters, the radius of the Field of View (FOV), R , is approximately 132.16 mm. The sampling intervals for X-ray spectra and mass attenuation coefficients are 1 keV. In the dual-spectral dual-material decomposition experiment, the IFBP and E-SART algorithms halt iteration when the difference in relative errors between adjacent iterations is less than 10^{-4} . IFBP uses Hamming filtering. Our method and network training parameters are as follows: encoding dimension $D = 8$, sampling step $l = 0.2581$, epochs=1200. The GPU used in the experiment is NVIDIA GeForce RTX 3080.

1) *Comparison Experiment with Noise-free Data:* In the noise-free comparison experiment, 720 projections were collected for each spectrum. Figure 5 presents the reconstruction results of the compared algorithms and our method using noise-free data. The first and second rows depict the density images of water and bone, respectively. The first, second, and third columns show the results reconstructed by IFBP, E-SART, and our method. It can be observed from the images that all three methods achieve satisfactory reconstruction results, with correct material separation. Notably, significant differences exist in the density images of water, as demonstrated by the profile plot along the 290th row in Fig. 6. From Fig. 6, it is evident that the profile plot of our method is closer to the Ground Truth. Table I provides quantitative metrics, including PSNR and SSIM. Among these, IFBP exhibits the highest PSNR, while our method demonstrates superior performance in terms of SSIM.

TABLE I
QUANTITATIVE COMPARISON OF RECONSTRUCTION QUALITY: SSIM AND PSNR METRICS FOR NOISE-FREE DATA EXPERIMENTS.

Noise-free data	IFBP		ESART		Ours	
	PSNR	SSIM	PSNR	SSIM	PSNR	SSIM
Bone	54.419	1.000	35.402	0.999	41.232	1.000
Water	40.975	0.976	31.968	0.975	39.434	0.999

2) *Comparison Experiment with Sparse Angle Data:* In this experiment, a comparison was conducted using sparse angle spectral data, with 120 projections collected for each spectrum. Figure 7 illustrates the reconstruction results of different algorithms using sparse angle data. The first and second rows display the density images of water and bone, respectively. The corresponding three columns present the reconstruction results of IFBP, E-SART, and our method. Observation of Fig. 7 reveals that IFBP and E-SART exhibit some radial artefacts in the water density image, which are challenging to eliminate even with more iterations. In contrast, our method shows no apparent artefacts in the reconstructed images. Significant differences are observed in the water density image; hence, the profile plot along the 290th row is provided in Fig. 8 for the compared algorithms and our method. It can be seen from Fig 8 that our method yields a profile plot closer to the Ground Truth for the water density image along the 290th row. Table II lists our method’s quantitative metrics, including PSNR and SSIM, and the compared algorithms. Regarding SSIM, our method exhibits no significant degradation relative to the metrics in Table I. Overall, our method achieved better reconstruction accuracy and fidelity under sparse angle spectral data.

TABLE II
QUANTITATIVE COMPARISON OF RECONSTRUCTION QUALITY: SSIM AND PSNR METRICS FOR SPARSE ANGLE DATA EXPERIMENTS.

Sparse angle	IFBP		ESART		Ours	
	PSNR	SSIM	PSNR	SSIM	PSNR	SSIM
Bone	49.7308	1.000	31.379	0.991	32.525	0.998
Water	30.5654	0.8913	25.0314	0.8967	31.695	0.991

3) *Comparison Experiment with Noisy Data:* The X-rays emitted by the X-ray source follow a Poisson distribution, where the number of photons detected along a certain path follows a Poisson distribution with a given mean value. To investigate the robustness of our method to noise, Poisson noise with an initial count of 10^6 photons was added to the noiseless data to simulate noisy multi-spectral projections. Figure 9 illustrates the reconstruction results of the compared algorithms and our method with Poisson noise data. Upon

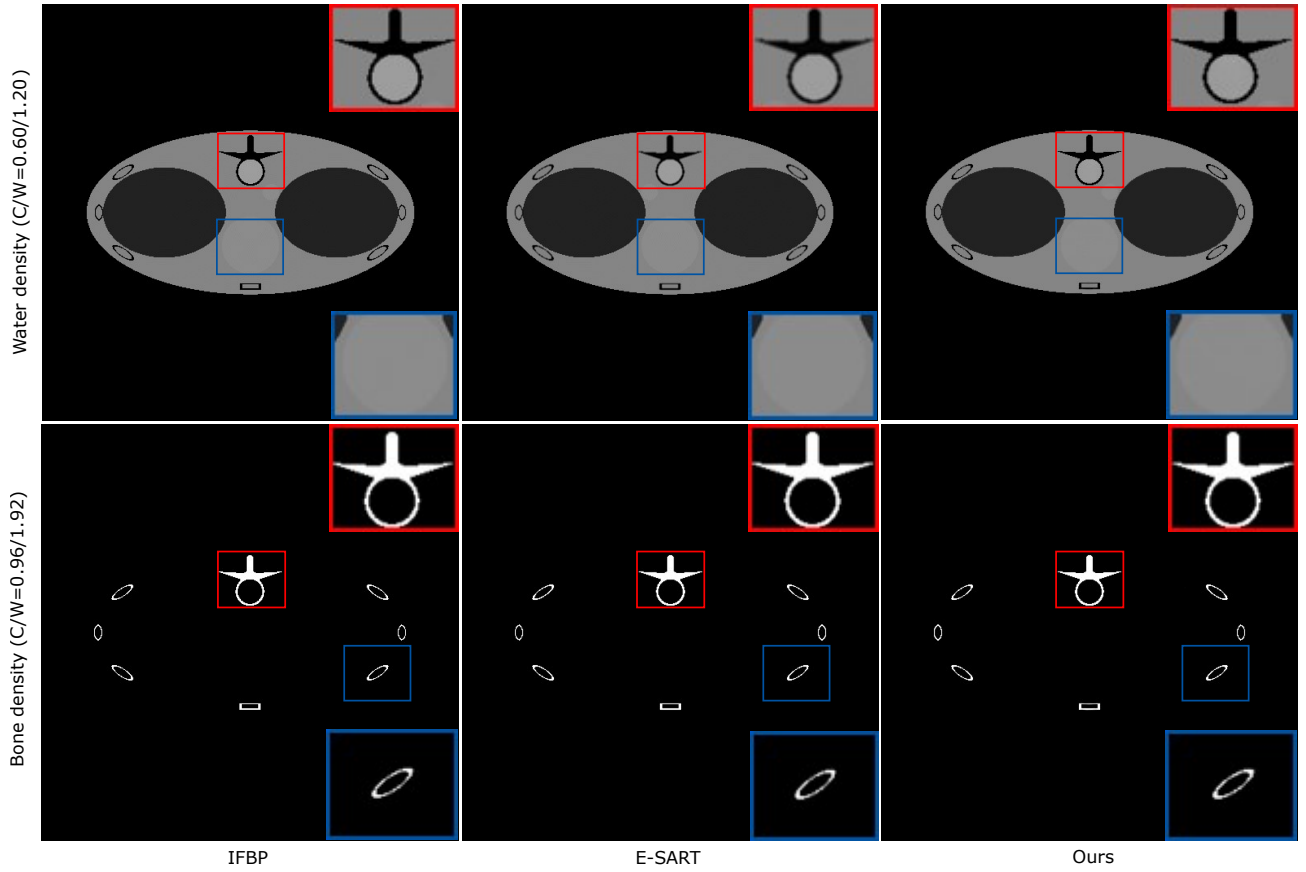


Fig. 5. Reconstruction results of the noise-free data experiments

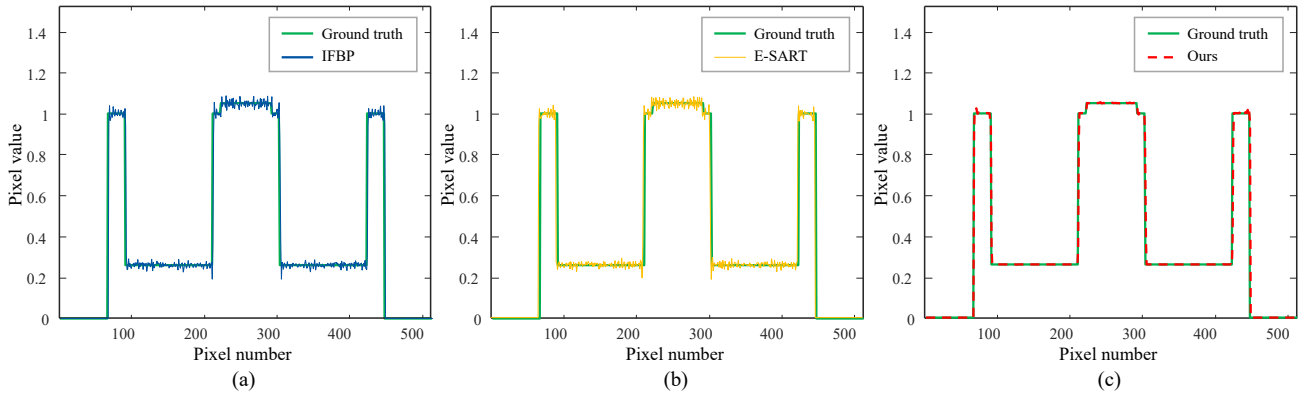


Fig. 6. Profiles at line 290: Water material images with the noise-free data experiments.

observing the reconstruction results, all three methods successfully achieved correct material separation. In Fig. 9, a local region is magnified within the red box, revealing that our method exhibits more explicit boundaries than E-SART and fewer artefacts than IFBP. Figure 10 provides profile plots along the 290th row for the compared algorithms and our method in the water density image. From the profile plots, it can be observed that our method yields smoother material image surfaces, which are closer to the Ground Truth. Table III

presents the quantitative metrics, including PSNR and SSIM. Our method performs best in terms of SSIM. Regarding PSNR, the IFBP algorithm achieves the highest score in the bone material density image but the lowest score in the water material density image. In contrast, Our method demonstrates similar PSNR scores for both bone and water, indicating a more stable performance and further substantiating the robustness of our approach to Poisson noise.

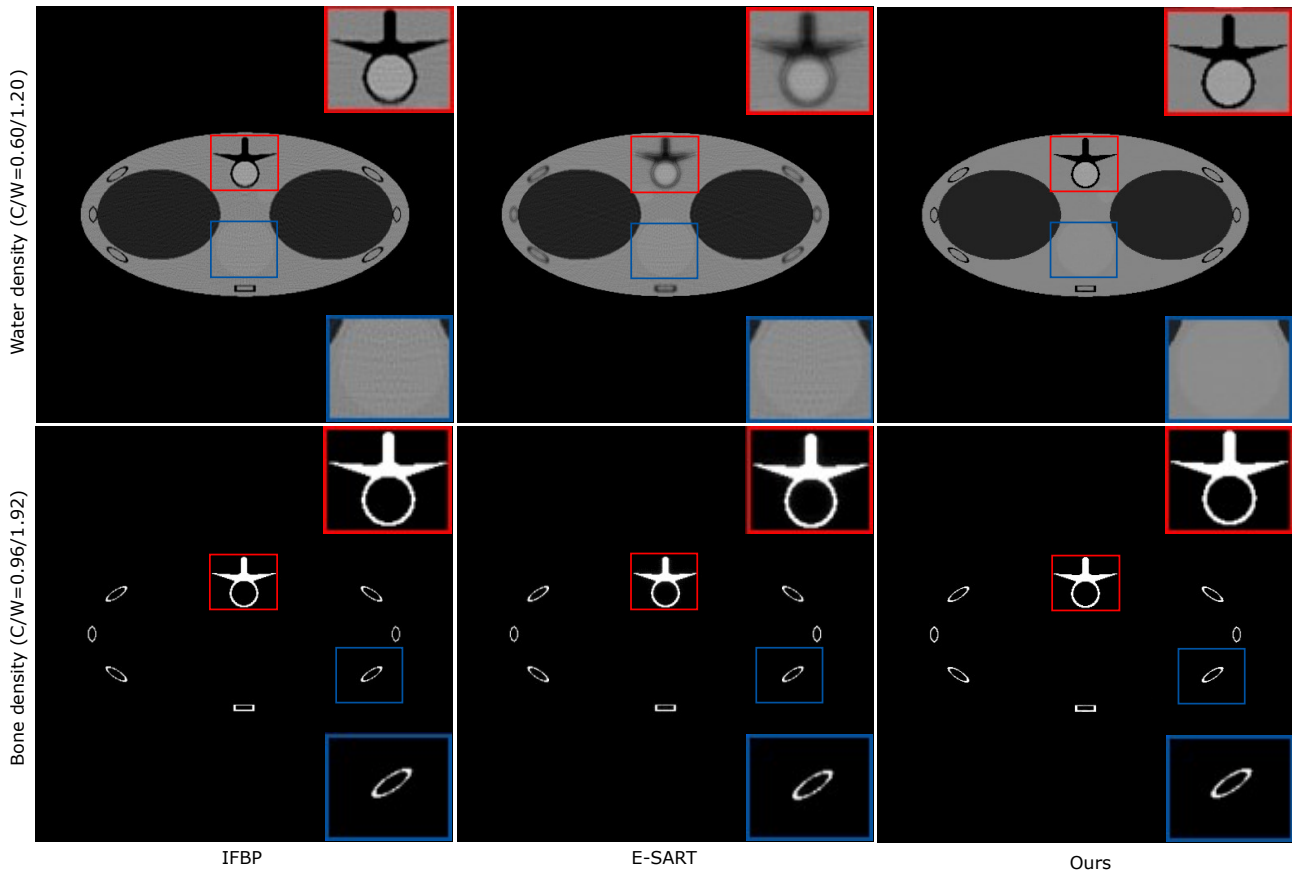


Fig. 7. Reconstruction results of the sparse angle data experiments

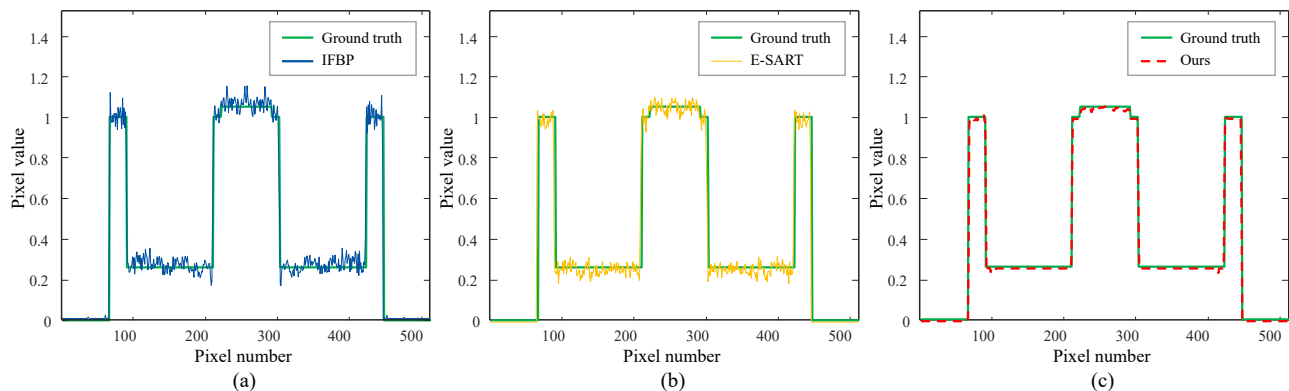


Fig. 8. Profiles at line 290: Water material images with the sparse angle data experiments.

TABLE III
QUANTITATIVE COMPARISON OF RECONSTRUCTION QUALITY: SSIM
AND PSNR METRICS FOR NOISE DATA EXPERIMENTS.

Noise data	IFBP		ESART		Ours	
	PSNR	SSIM	PSNR	SSIM	PSNR	SSIM
Bone	42.764	0.940	35.422	0.997	32.242	0.997
Water	26.234	0.642	31.536	0.937	31.330	0.990

4) *Comparison Experiment with Noise and Geometric Inconsistency data:* This subsection aims to verify the robustness of our method in dealing with noise and geometric inconsistency during the acquisition of spectral CT data. Regarding noise, we added Poisson noise with an initial count of 10^6 photons, following the same procedure as before. To simulate geometrically inconsistent projection data, we collected data with 1441 projection angles, rotating the X-ray source once per energy spectrum. For the 80 keV spectrum, we collected

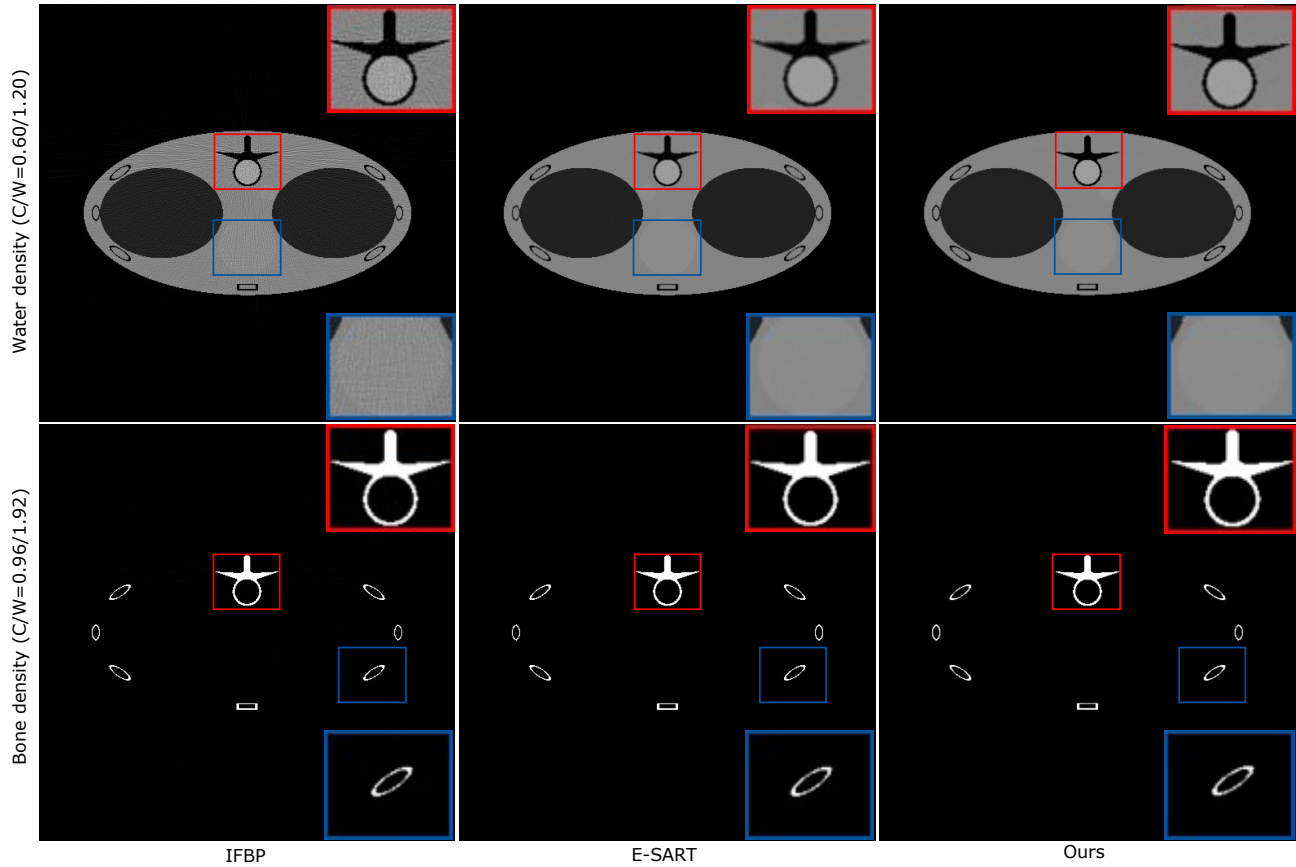


Fig. 9. Reconstruction results of the noise data experiments

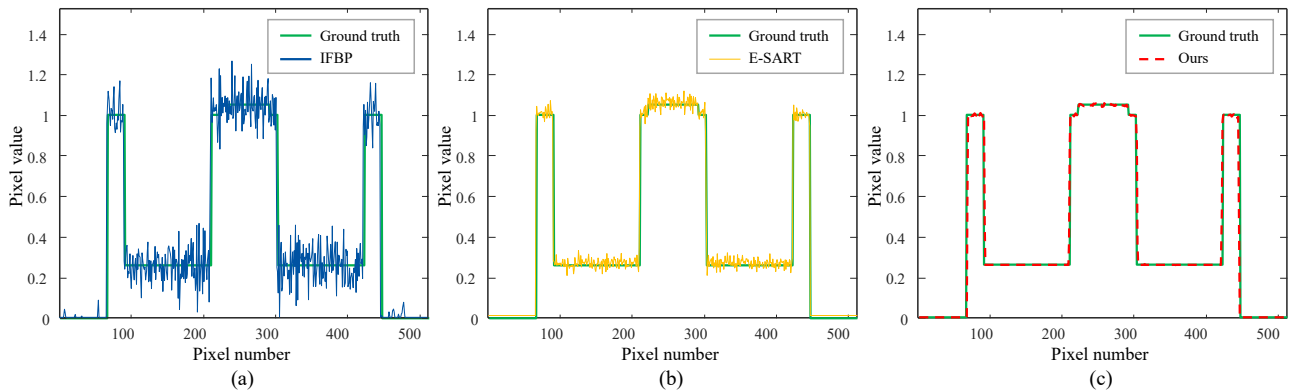


Fig. 10. Profiles at line 290: Water material images with the noise data experiments.

projections at every other angle starting from angle 0, resulting in 720 projection angles. Similarly, for the 140 keV spectrum, we collected projections at every other angle starting from angle 1, resulting in 720 projection angles.

Figure 11 illustrates the reconstruction results of the compared algorithms and our method with Poisson noise and geometrically inconsistent data. Upon observing the reconstruction results, all three methods achieve good reconstruction performance. However, our method exhibits fewer artefacts in

the water material density image. Figure 12 provides profile plots along the 290th row for both the compared algorithms and our method in the water material density image. From the profile plots, it can be seen that our method yields smoother material image surfaces, which are closer to the Ground Truth. Table III lists the quantitative metrics, including PSNR and SSIM. Our method performs the best in terms of SSIM.

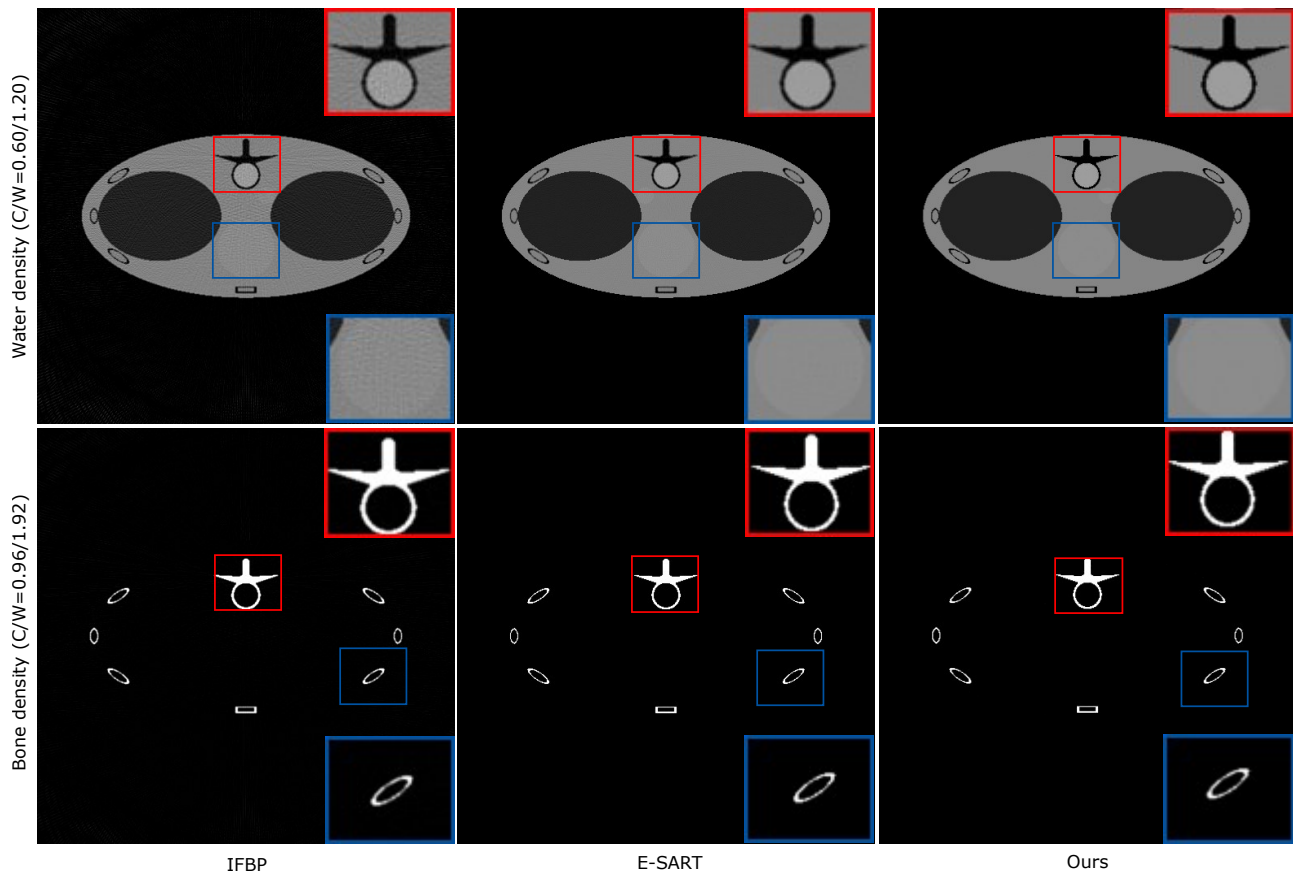


Fig. 11. Reconstruction results of the noise and geometric inconsistency experiments

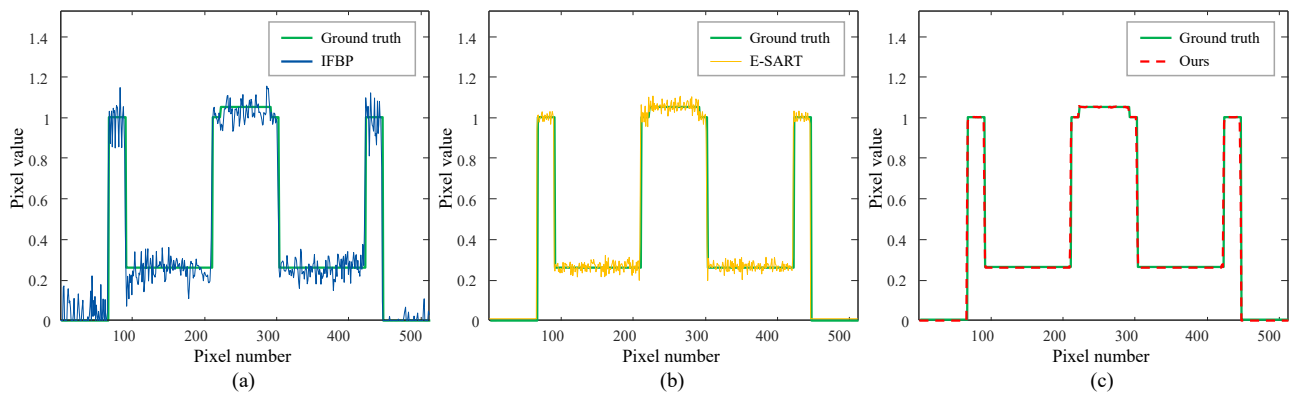


Fig. 12. Profiles at line 290: Water material images with noise and geometric inconsistencies.

TABLE IV
QUANTITATIVE COMPARISON OF RECONSTRUCTION QUALITY: SSIM
AND PSNR METRICS FOR NOISE AND GEOMETRIC INCONSISTENCY
DATA EXPERIMENTS.

Geometric inconsistency	IFBP		ESART		Ours	
	PSNR	SSIM	PSNR	SSIM	PSNR	SSIM
Bone	42.764	0.940	35.264	0.998	32.815	0.998
Water	26.234	0.642	30.867	0.936	31.806	0.994

B. Single-Spectrum Dual-Material Decomposition Experiments

This section aims to validate the effectiveness of our algorithm in handling ill-posed and underdetermined equation systems. In this experiment, CT reconstruction of dual materials was achieved using X-ray scans with a single spectrum, specifically $M = 2$ and $K = 1$. We conducted projection simulations for X-ray spectra over 2π radians, resulting in 720 projections, with detailed system parameter settings described

in the previous section.

Figure 13 illustrates the experiments conducted to fit the neural field for water-bone materials under an 80 kVp spectrum. From the figure, it can be observed that our method successfully separates the water and bone materials even under a single spectrum, resulting in good reconstruction results. Figure 14 displays profile plots of our proposed method along the 290th row in the water density image, showing a close match to the Ground Truth. Table V presents the quantitative metrics, including PSNR and SSIM, which demonstrate certain advantages compared to the performance of our proposed algorithm in dual spectrum dual material decomposition (see Table I).

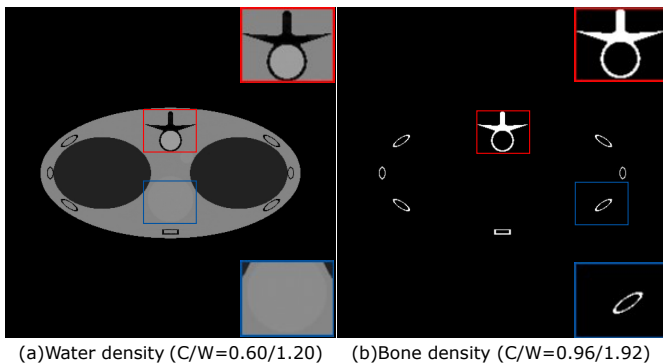


Fig. 13. Reconstructed results from single spectrum (80 kVp) dual material decomposition experiments.

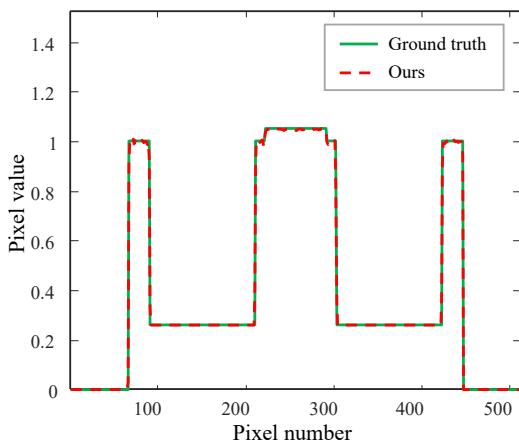


Fig. 14. Profiles at line 290: Water material images with single spectrum (80 kVp) dual material decomposition experiments.

C. High-Resolution Base Material Image Reconstruction Experiments

Our algorithm reconstructs continuous material images by sampling rays, providing a unique advantage not limited by the CT system matrix. It can extract high-resolution reconstruction images from well-trained networks, meeting the demands for high-resolution reconstruction.

TABLE V
QUANTITATIVE COMPARISON OF RECONSTRUCTION QUALITY: SSIM AND PSNR METRICS FOR SINGLE-SPECTRUM DUAL-MATERIAL DECOMPOSITION EXPERIMENTS.

Single spectrum (80 KeV)	PSNR	SSIM
Bone	43.983	1.000
Water	39.048	0.999

Figure 15 displays different-sized reconstruction images extracted from noise-free data in Fig. 5 after training the network. The images in the figure have been scaled to different resolutions. To analyze the quality of the reconstruction images extracted by our algorithm more intuitively, the Ground Truth was subjected to Bilinear interpolation to obtain images at corresponding resolutions, and Profile plots were drawn in Fig. 16.

In Fig. 16, where the curves jump, the curve of the reconstruction image closely matches the curve of the Bicubic image, indicating that the images extracted from the network by our algorithm are not affected by resolution.

Table VI provides the PSNR and SSIM values of the extracted images at different resolutions than the Bilinear images. The PSNR values decrease with increasing resolution, possibly due to noise introduced by Bilinear interpolation. In contrast, the SSIM values are relatively stable, reflecting the high quality of the reconstruction images extracted by our algorithm.

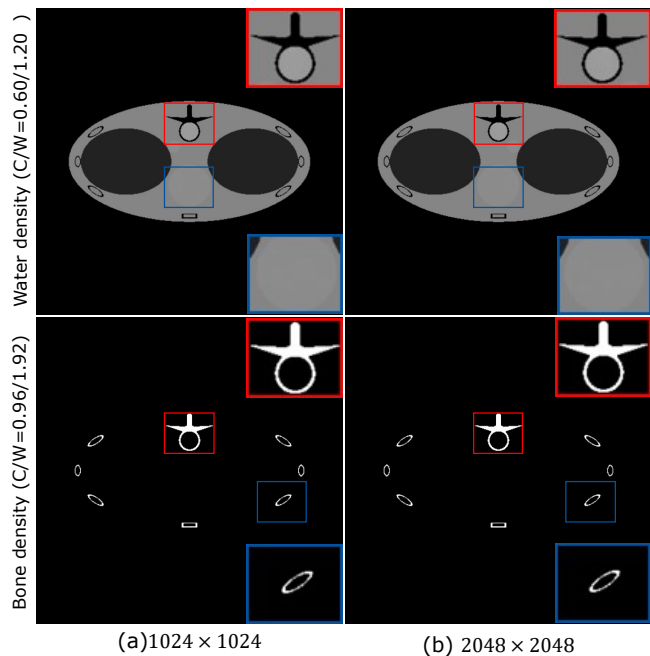


Fig. 15. Experimental results obtained from the neural base-material field at varying resolutions, where the image dimensions progress from left to right as 1024×1024 , 2048×2048 pixels, respectively.

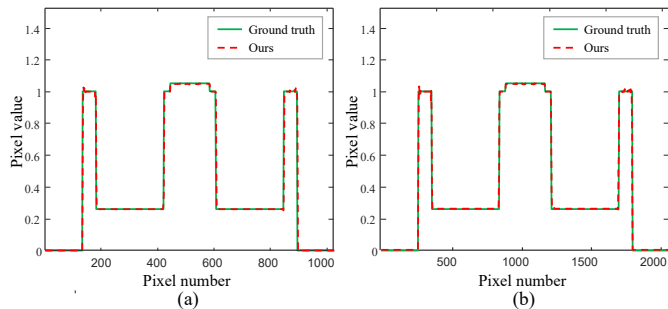


Fig. 16. Profiles of water at resolutions of $1024 \times 1024, 2048 \times 2048$ pixels extracted from the neural base-material field. (a) 580 Lines, (b) 1160 Lines.

TABLE VI
QUANTITATIVE COMPARISON OF SSIM AND PSNR METRICS AT
RESOLUTIONS OF $1024 \times 1024, 2048 \times 2048$ PIXELS

Noise-free data	1024×1024		2048×2048	
	PSNR	SSIM	PSNR	SSIM
Bone	40.072	0.999	37.245	0.998
Water	38.393	0.997	35.902	0.995

V. DISCUSSIONS

In this study, we have used a novel approach to achieve spectral CT base material decomposition. We treat base materials as continuous 3D implicit functions of coordinates and represent them using fully connected deep neural networks. In our numerical simulation experiments of dual-spectral dual-material decomposition, we considered various scenarios, such as noise-free data, sparse angles, Poisson noise, and geometric inconsistency. Compared to traditional methods like E-SART and IFBP, our approach performs better in handling sparse angle and Poisson noise data. This indicates that our method is robust enough to address challenges that may arise in practical applications.

Furthermore, we parameterized the water-bone materials under an 80 kVp spectrum in the single-spectral dual-material decomposition experiments. The results demonstrate that our method can effectively separate water and bone materials even under single-spectral conditions, showcasing its ability to tackle ill-posed and underdetermined equations.

The experiment on high-resolution material reconstruction demonstrates that our method can generate high-resolution material density images from well-trained networks. The quantitative evaluation of the reconstructed high-resolution material density images indicates that our algorithm performs excellently in reconstructing high-resolution density images and is not constrained by traditional CT system matrices.

Our method has several advantages. It features a lightweight network structure with fewer model parameters and adopts a self-supervised learning approach without relying on ad-

ditional datasets. However, it also has some limitations. For example, training fully connected neural networks to parameterize decomposed material after objects requires long training times and high memory requirements in the auto-differentiation framework. Therefore, future research will focus on improving network structures, optimizing training strategies, and accelerating techniques to reduce training time and memory requirements. This will further enhance the practicality and efficiency of the algorithm.

VI. CONCLUSION

This study utilizes a parametric neural field model for spectral CT material decomposition. At the core of this model is the conceptualization of materials as continuous vector-valued implicit functions of coordinates. To achieve material decomposition reconstruction, we utilize the auto-differentiation framework in deep learning to train a fully connected neural network capable of generating material density images of arbitrary high resolution. As a self-supervised model, this method offers significant advantages by eliminating the need for external datasets for training.

In contrast to traditional spectral CT decomposition algorithms, our approach avoids discretizing the imaging space during the forward modelling process. This simplification greatly simplifies the complex computations involved in solving inverse problems. Not only does it enhance computational efficiency, but it also increases the applicability and flexibility of the model. The experimental results indicate that our approach holds tremendous potential in addressing the material decomposition challenges in spectral CT technology.

ACKNOWLEDGMENTS

Thanks to Associate Professor Xiaojuan Deng’s feedback during the manuscript revision and PhD Huiying Pan’s help with the dual-spectral reconstruction.

REFERENCES

- [1] W. Perman and J. Vetter, “Evaluation of a prototype dual-energy computed tomographic apparatus. i. phantom studies,” *Medical physics*, vol. 13, no. 3, pp. 334–339, 1986.
- [2] T. Niu, X. Dong, M. Petrongolo, and L. Zhu, “Iterative image-domain decomposition for dual-energy ct,” *Medical physics*, vol. 41, no. 4, p. 041901, 2014.
- [3] B. Mildenhall, P. P. Srinivasan, M. Tancik, J. T. Barron, R. Ramamoorthi, and R. Ng, “Nerf: Representing scenes as neural radiance fields for view synthesis,” *Communications of the ACM*, vol. 65, no. 1, pp. 99–106, 2021.
- [4] R. A. BROOKS and G. D. CHIRO, “Beam hardening in x-ray reconstructive tomography,” *Physics in medicine & biology*, vol. 21, no. 3, p. 390, 1976.
- [5] Y. Xue, R. Ruan, X. Hu, Y. Kuang, J. Wang, Y. Long, and T. Niu, “Statistical image-domain multimaterial decomposition for dual-energy ct,” *Medical physics*, vol. 44, no. 3, pp. 886–901, 2017.
- [6] D. Wu, L. Zhang, X. Zhu, X. Xu, and S. Wang, “A weighted polynomial based material decomposition method for spectral x-ray ct imaging,” *Physics in Medicine & Biology*, vol. 61, no. 10, p. 3749, 2016.

- [7] C. Maaß, M. Baer, and M. Kachelrieß, "Image-based dual energy ct using optimized precorrection functions: A practical new approach of material decomposition in image domain," *Medical physics*, vol. 36, no. 8, pp. 3818–3829, 2009.
- [8] A. Coleman and M. Sinclair, "A beam-hardening correction using dual-energy computed tomography," *Physics in medicine & biology*, vol. 30, no. 11, p. 1251, 1985.
- [9] Z. Ying, R. Naidu, and C. R. Crawford, "Dual energy computed tomography for explosive detection," *Journal of X-ray Science and Technology*, vol. 14, no. 4, pp. 235–256, 2006.
- [10] E. Y. Sidky, Y. Zou, and X. Pan, "Impact of polychromatic x-ray sources on helical, cone-beam computed tomography and dual-energy methods," *Physics in Medicine & Biology*, vol. 49, no. 11, p. 2293, 2004.
- [11] P. Stenner, T. Berkus, and M. Kachelrieß, "Empirical dual energy calibration (edec) for cone-beam computed tomography," *Medical physics*, vol. 34, no. 9, pp. 3630–3641, 2007.
- [12] K.-S. Chuang and H. Huang, "Comparison of four dual energy image decomposition methods," *Physics in Medicine & Biology*, vol. 33, no. 4, p. 455, 1988.
- [13] Y. Zhao, X. Zhao, and P. Zhang, "An extended algebraic reconstruction technique (e-art) for dual spectral ct," *IEEE transactions on medical imaging*, vol. 34, no. 3, pp. 761–768, 2014.
- [14] J. Hu, X. Zhao, and F. Wang, "An extended simultaneous algebraic reconstruction technique (e-sart) for x-ray dual spectral computed tomography," *Scanning*, vol. 38, no. 6, pp. 599–611, 2016.
- [15] M. Li, Y. Zhao, and P. Zhang, "Accurate iterative fbp reconstruction method for material decomposition of dual energy ct," *IEEE transactions on medical imaging*, vol. 38, no. 3, pp. 802–812, 2018.
- [16] H. Pan, S. Zhao, W. Zhang, H. Zhang, and X. Zhao, "Fast iterative reconstruction for multi-spectral ct by a schmidt orthogonal modification algorithm (soma)," *Inverse Problems*, vol. 39, no. 8, p. 085001, 2023.
- [17] B. Zhu, J. Z. Liu, S. F. Cauley, B. R. Rosen, and M. S. Rosen, "Image reconstruction by domain-transform manifold learning," *Nature*, vol. 555, no. 7697, pp. 487–492, 2018.
- [18] J. F. Abascal, N. Ducros, V. Pronina, S. Rit, P.-A. Rodesch, T. Broussaud, S. Bussod, P. C. Douek, A. Hauptmann, and S. Arridge, "Material decomposition in spectral ct using deep learning: a sim2real transfer approach," *IEEE Access*, vol. 9, pp. 25 632–25 647, 2021.
- [19] W. Zhang, H. Zhang, L. Wang, X. Wang, X. Hu, A. Cai, L. Li, T. Niu, and B. Yan, "Image domain dual material decomposition for dual-energy ct using butterfly network," *Medical physics*, vol. 46, no. 5, pp. 2037–2051, 2019.
- [20] D. P. Clark, M. Holbrook, and C. T. Badea, "Multi-energy ct decomposition using convolutional neural networks," in *Medical Imaging 2018: Physics of Medical Imaging*, vol. 10573. SPIE, 2018, pp. 415–423.
- [21] Z. Shi, H. Li, Q. Cao, Z. Wang, and M. Cheng, "A material decomposition method for dual-energy ct via dual interactive wasserstein generative adversarial networks," *Medical Physics*, vol. 48, no. 6, pp. 2891–2905, 2021.
- [22] H. Gong, S. Tao, K. Rajendran, W. Zhou, C. H. McCollough, and S. Leng, "Deep-learning-based direct inversion for material decomposition," *Medical physics*, vol. 47, no. 12, pp. 6294–6309, 2020.
- [23] W. Cong, Y. Xi, P. Fitzgerald, B. De Man, and G. Wang, "Virtual monoenergetic ct imaging via deep learning," *Patterns*, vol. 1, no. 8, 2020.
- [24] A. Mittal, "Neural radiance fields: Past, present, and future," *arXiv preprint arXiv:2304.10050*, 2023.
- [25] A. Chen, Z. Xu, A. Geiger, J. Yu, and H. Su, "Tensorf: Tensorial radiance fields," in *European Conference on Computer Vision*. Springer, 2022, pp. 333–350.
- [26] Y. Xie, T. Takikawa, S. Saito, O. Litany, S. Yan, N. Khan, F. Tombari, J. Tompkin, V. Sitzmann, and S. Sridhar, "Neural fields in visual computing and beyond," in *Computer Graphics Forum*, vol. 41, no. 2. Wiley Online Library, 2022, pp. 641–676.
- [27] Y. Sun, J. Liu, M. Xie, B. Wohlberg, and U. S. Kamilov, "Coil: Coordinate-based internal learning for tomographic imaging," *IEEE Transactions on Computational Imaging*, vol. 7, pp. 1400–1412, 2021.
- [28] G. Zang, R. Idoughi, R. Li, P. Wonka, and W. Heidrich, "Intratomo: self-supervised learning-based tomography via sinogram synthesis and prediction," in *Proceedings of the IEEE/CVF International Conference on Computer Vision*, 2021, pp. 1960–1970.
- [29] D. Rückert, Y. Wang, R. Li, R. Idoughi, and W. Heidrich, "Neat: Neural adaptive tomography," *ACM Transactions on Graphics (TOG)*, vol. 41, no. 4, pp. 1–13, 2022.
- [30] L. Shen, J. Pauly, and L. Xing, "Nerp: implicit neural representation learning with prior embedding for sparsely sampled image reconstruction," *IEEE Transactions on Neural Networks and Learning Systems*, 2022.
- [31] A. W. Reed, H. Kim, R. Anirudh, K. A. Mohan, K. Champley, J. Kang, and S. Jayasuriya, "Dynamic ct reconstruction from limited views with implicit neural representations and parametric motion fields," in *Proceedings of the IEEE/CVF International Conference on Computer Vision*, 2021, pp. 2258–2268.
- [32] R. Zha, Y. Zhang, and H. Li, "Naf: Neural attenuation fields for sparse-view cbct reconstruction," in *International Conference on Medical Image Computing and Computer-Assisted Intervention*. Springer, 2022, pp. 442–452.
- [33] F. Vasconcelos, B. He, N. Singh, and Y. W. Teh, "Uncertain: Uncertainty quantification of end-to-end implicit neural representations for computed tomography," *arXiv preprint arXiv:2202.10847*, 2022.
- [34] K. Hornik, M. Stinchcombe, and H. White, "Multilayer feedforward networks are universal approximators," *Neural Networks*, vol. 2, no. 5, pp. 359–366, 1989.
- [35] N. Rahaman, A. Baratin, D. Arpit, F. Draxler, M. Lin, F. Hamprecht, Y. Bengio, and A. Courville, "On the spectral bias of neural networks," in *International conference on machine learning*. PMLR, 2019, pp. 5301–5310.
- [36] M. Tancik, B. Mildenhall, T. Wang, D. Schmidt, P. P. Srinivasan, J. T. Barron, and R. Ng, "Learned initializations for optimizing coordinate-based neural representations," in *Proceedings of the IEEE/CVF Conference on Computer Vision and Pattern Recognition*, 2021, pp. 2846–2855.
- [37] V. Sitzmann, J. Martel, A. Bergman, D. Lindell, and G. Wetzstein, "Implicit neural representations with periodic activation functions," *Advances in neural information processing systems*, vol. 33, pp. 7462–7473, 2020.
- [38] Z. Chen, Z. Li, L. Song, L. Chen, J. Yu, J. Yuan, and Y. Xu, "Neurbf: A neural fields representation with adaptive radial basis functions," in *Proceedings of the IEEE/CVF International Conference on Computer Vision*, 2023, pp. 4182–4194.